

14 **Abstract**

15 The interaction of sub-surface, gravity-driven flows with inclusions of different perme-
 16 abilities are investigated theoretically using a model that exploits the relative shallow-
 17 ness of the motion. Numerically computed solutions for steady motion around cylindrical
 18 inclusions reveal a range of behaviours dependent on the ratio of the interior to ex-
 19 terior permeability and a dimensionless flow parameter that measures the far-field thick-
 20 ness to the product of the gradient of the slope down which the fluid flows and the width
 21 of the inclusion. When the inclusion is relatively narrow, the depth of the flow is little
 22 changed from its far-field value and the fluid is focussed into inclusions of higher per-
 23 meability and deflected around those of lower permeability. However, if the inclusion is
 24 relatively wide then three qualitatively different regimes emerge, dependent on the ra-
 25 tio of permeabilities. When the interior and exterior permeabilities are similar, then neg-
 26 ligible deviation of the flow occurs apart from within thin transition layers at the bound-
 27 ary of the inclusion. When the permeabilities differ significantly, the flow forms deep ponds
 28 at either the upstream or downstream boundary of the inclusion for relatively low or high
 29 permeability inclusion, respectively, which arise due to deflection or focussing. In each
 30 case, asymptotic relationships are derived between the depth of the flow and the param-
 31 eters. Inclusions of differing cross-section are also analysed numerically and analytically
 32 to draw out the interplay between adjustment, deflection and focussing.

33 **1 Introduction**

34 Gravity-driven flows in porous media occur in a wide range of industrial and en-
 35 vironmental contexts including hydrology, carbon dioxide storage, geothermal power gen-
 36 eration and contaminant leaks (Bear, 1971; MacFarlane et al., 1983; Guo et al., 2016).
 37 These sub-surface flows are difficult to monitor directly and therefore it is common to
 38 drill wells to sample the flow, for example in CO₂ storage projects to monitor break-through
 39 times (Mathieson et al., 2011; Hannis et al., 2015). Wells are also used for extracting fresh
 40 water from aquifers and for monitoring salt water intrusion (Dagan & Zeitoun, 1998; Mas-
 41 terson et al., 1998; Barlow & Reichard, 2010). Accurately determining the flow veloc-
 42 ity from a single borehole presents difficulties, however, because its presence may signif-
 43 icantly alter the flow field even in the case that no fluid is extracted because it alters the
 44 structure and permeability of the constituent porous media (Sekhar & Sano, 2001). It
 45 is vital to understand this effect in order to interpret the data acquired correctly.

46 It is well-established that pressure-driven flows are focused by inclusions that are
 47 of higher permeability than the surroundings whilst lower permeability inclusions divert
 48 the flow, and the volume flux of fluid that passes through the inclusion has been calcu-
 49 lated in each case (Hinch & Bhatt, 1990; Phillips, 1991). However, in many contexts, the
 50 flow forms a free-surface and is primarily driven by buoyancy. We develop a physical model
 51 to explore the interaction of free-surface flows driven by gravity (rather than by imposed
 52 pressure gradients) on an inclined plane with a cylindrical inclusion of different perme-
 53 ability (figure 1). We investigate how the flow thickness and velocity field depend on the
 54 permeability ratio and the width of the cylinder relative to the oncoming flow thickness
 55 and slope inclination. In the case of a relatively narrow cylinder, we show that the be-
 56 haviour is analogous to the interaction of two-dimensional pressure-driven flows with in-
 57 clusions. The interaction with relatively wide cylinders is substantially different, how-
 58 ever. For example, we will show that upstream of a relatively wide impermeable inclu-
 59 sion, deep ponds of fluid will form. Similar behaviour occurs on the downstream side of
 60 the interior of a high permeability inclusion. We are particularly interested in the flux
 61 of fluid into the cylinder from upstream and determining controls on whether the par-
 62 ticle paths are predominantly diverted around, focused into or not significantly influenced
 63 by the cylindrical inclusion. Another aim is to determine the occurrence, depth and lo-
 64 cation of ponded regions in which the free-surface is approximately horizontal, the fluid
 65 is nearly stationary and the flow depth is much greater than its upstream value.

66 The present analysis has important applications for geologic CO₂ sequestration.
 67 The flow of the stored CO₂ is driven by buoyancy away from the injection well. The CO₂
 68 is likely to contact abandoned wells, which may act as high or low permeability inclu-
 69 sions and Celia et al. (2005) showed that they could significantly influence the motion
 70 of the plume and present a key leakage risk (see also Nordbotten et al., 2004). In addi-
 71 tion, the CO₂ may encounter natural heterogeneous inclusions owing to fractures in the
 72 rock, through which CO₂ may also leak (Pritchard, 2007; Woods & Norris, 2010). The
 73 CO₂ preferentially migrates through high permeability regions, which may increase the
 74 distance travelled and reduce the storage efficiency (Di Donato & Blunt, 2004).

75 Tracers are sometimes added to subsurface flows to monitor breakthrough times
 76 and constrain aquifer properties (Stalker et al., 2015) and rock heterogeneity is known
 77 to have a strong effect on the migration of tracers in a porous medium (Dagan, 1984;
 78 Werth et al., 2006). Indeed, it has been shown that inclusions of different permeability
 79 can totally dominate dispersion in a pressure-driven flow owing to the different speeds
 80 of particles that pass through the inclusion (Eames & Bush, 1999). In the context of free-
 81 surface flows, Hinton and Woods (2019) showed that vertical variations in permeabil-
 82 ity can lead to complex interactions between dispersing tracer and the interface. In this
 83 study, we use our results to calculate the paths taken as particles pass through and around
 84 the cylinder for the different flow regimes that occur depending on the relative perme-
 85 ability and width of the inclusion.

86 We begin our analysis in §2, where we formulate a shallow model for the flow using
 87 Darcy’s law and we identify that the problem has two dimensionless parameters: the
 88 ratio of the permeabilities inside and outside a circular cylinder and the flow param-
 89 eter, which is the ratio of the oncoming flow thickness to the product of the cylinder ra-
 90 dius and the slope gradient. In §3, we consider the regime of a relatively narrow cylin-
 91 der, which slightly perturbs the flow depth. Asymptotic predictions for the flow thick-
 92 ness inside and outside the cylinder are calculated. This identifies that if the cylinder
 93 has lower permeability than the surrounding medium then the flow is diverted around
 94 the cylinder and the maximum thickness occurs on the upstream boundary of the cylin-
 95 der and the converse occurs for a cylinder of higher permeability.

96 We consider relatively wide obstructions in §4. In contrast to the ‘narrow’ regime,
 97 the interaction with a wide obstruction is qualitatively sensitive to the permeability ra-
 98 tio. When this ratio is of order unity, the particle paths are parallel to the downslope
 99 direction passing straight through the cylinder. The velocity changes as particles enter
 100 the cylinder and mass conservation requires that the depth is constant outside the cylin-
 101 der but a different constant inside the cylinder. However, if the cylinder is sufficiently
 102 impermeable (§5) then fluid ponds upstream of the cylinder. The oncoming flow is pre-
 103 dominantly diverted around the cylinder. This behaviour is similar to the interaction of
 104 buoyant plumes with low permeability layers, which leads to lateral spreading before the
 105 fluid drains through the layer (Sahu & Flynn, 2017; Hewitt et al., 2020). In the case that
 106 the cylinder is of sufficiently high permeability relative to the exterior, the flow within
 107 the cylinder is focused towards a pond at the most downstream point (§6). The flow out
 108 of the cylinder occurs predominantly through this pond. In §7, we generalise the results
 109 to some cylinders with non-circular cross-sections to draw out some of the features that
 110 determine the location and magnitude of the ponds. We consider the implications of our
 111 results for some subsurface flows in §8. Concluding remarks are made in §9.

112 2 Formulation

113 We analyse the gravitationally-driven steady flow of a fluid of dynamic viscosity
 114 μ in a saturated, deep porous medium, which is bounded below by an impermeable plane
 115 at an angle β to the horizontal (figure 1). The coordinate axes are orthogonal with X
 116 aligned to steepest descent along the sloping boundary and Z perpendicular to the bound-

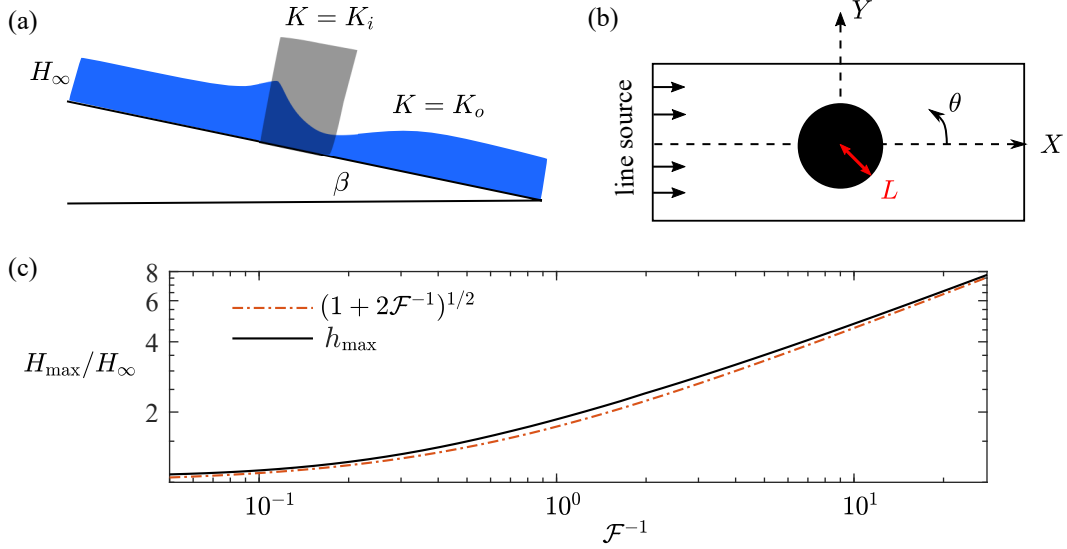


Figure 1: (a) Side view of the flow showing the far upstream thickness, H_∞ . (b) Bird's eye view of the setup. (c) The maximum flow depth, $h_{\max} = H_{\max}/H_\infty$ as a function of the flow parameter, \mathcal{F} for an impermeable circular cylinder.

117 ary. The steady flow thickness is given by $Z = H(X, Y)$. We assume throughout that
 118 the flow is 'shallow'; the velocity in the Z direction is negligible relative to the velocity
 119 in the X and Y directions. Under this 'lubrication' approximation, the excess pressure
 120 within the fluid is hydrostatic (Bear, 1971; Huppert & Woods, 1995),

$$P = \Delta\rho g[H(X, Y) - Z] \cos \beta, \quad (1)$$

121 where $\Delta\rho$ is the density difference between the intruding fluid and the ambient. The Darcy
 122 velocity is given by (Bear, 1971; Vella & Huppert, 2006)

$$\mathbf{U} = -\frac{K(R)\Delta\rho g}{\mu} \left(-\sin \beta + \cos \beta \frac{\partial H}{\partial X}, \cos \beta \frac{\partial H}{\partial Y} \right), \quad (2)$$

123 where $R = |\mathbf{X}|$ and the permeability of the medium, $K(R)$, may take different constant
 124 values inside and outside the cylinder, which is of radius L ,

$$K(R) = \begin{cases} K_i, & R < L, \\ K_o, & R > L. \end{cases} \quad (3)$$

125 We analyse the injection of fluid at a constant flux per unit width, Q , from a line source
 126 far upstream. Away from the cylinder, the steady flow depth is a constant, given by (Huppert
 127 & Woods, 1995)

$$H_\infty = \frac{\mu\phi Q}{\Delta\rho g K_o \sin \beta}, \quad (4)$$

128 where ϕ is the porosity, assumed to be constant. In the case that the input fluid is the
 129 non-wetting phase (such as in CO_2 sequestration) there may be a significant 'capillary
 130 entry pressure' that must be exceeded for the input fluid to invade regions of low per-
 131 meability or porosity (Bear & Ryzhik, 1998; Bachu, 2015). This entry pressure is asso-
 132 ciated with the effects of interfacial tension between the fluids restricting flow through
 133 the pore throats and is approximately given by (Purcell, 1949)

$$P_c = \frac{2\sigma \cos \alpha}{D}, \quad (5)$$

134 where D is the maximum pore throat radius, α is the contact angle and σ represents in-
 135 terfacial tension. The hydrostatic pressure at the edge of the cylinder must exceed P_c ,
 136 which corresponds to the following condition on the flow depth (Woods & Farcas, 2009),

$$H > H_c = \frac{P_c}{\Delta\rho g \cos \beta}. \quad (6)$$

137 Typical values of the capillary entry pressure for low permeability shales in the context
 138 of CO₂ sequestration are $P_c = 0.5\text{--}5\text{MPa}$ (Chiquet et al., 2007; Kuila & Prasad, 2013;
 139 Rezaeyan et al., 2015), which with a density difference of 300kg m^{-3} implies that the flow
 140 depth must exceed approximately $H_c = 300$ metres. In figure 1c, the maximum flow
 141 depth at the boundary of an impermeable cylinder relative to the upstream depth, H_{\max}/H_∞
 142 is plotted as a function of the flow parameter, \mathcal{F} (defined below in (9)). Typical flows
 143 in subsurface aquifers have thicknesses of up to tens of metres and thus we anticipate
 144 that even given an increase in depth near the cylinder, inclusions of such low permeabil-
 145 ity are never invaded. In the calculations that follow, we examine the flow fields and thick-
 146 nesses for inclusions that are of greater and smaller permeabilities than the surround-
 147 ings, noting that if $H_{\max} < H_c$ then the inclusion may be modelled as impermeable.

148 We use the following scalings to non-dimensionalise the problem,

$$h = H/H_\infty, \quad x = X/L, \quad y = Y/L \quad \text{and} \quad r = R/L. \quad (7)$$

149 The dimensionless flux is simply the product of the in-plane velocities with the flow thick-
 150 ness, $\mathbf{q} = \int_0^h (u, v) dz = (uh, vh)$, since u and v are independent of z . The flux may
 151 be expressed as

$$\mathbf{q} = k(r)h \left(1 - \mathcal{F} \frac{\partial h}{\partial x}, -\mathcal{F} \frac{\partial h}{\partial y} \right), \quad (8)$$

152 where $k(r) = 1$ in $r > 1$ and $k(r) = \lambda = K_i/K_o$ in $r < 1$. The dimensionless problem
 153 is governed by two parameters: the permeability ratio and the flow parameter;

$$\lambda = \frac{K_i}{K_o}, \quad \mathcal{F} = \frac{H_\infty}{L \tan \beta}, \quad (9)$$

154 both of which may feasibly vary over a wide range of values. The flow parameter, \mathcal{F} , mea-
 155 sures the thickness of the oncoming flow relative to the lengthscale of the cylindrical in-
 156 clusion and the inclination of the underlying boundary. In this way it is the ratio of the
 157 flow driven by gradients of the hydrostatic pressure ($\Delta\rho g K \cos \beta H / [\mu L]$) to the flow driven
 158 by gravity downslope ($\Delta\rho g K \sin \beta / \mu$).

159 Since the flow is steady, mass conservation is given by requiring that the divergence
 160 of the flux (8) vanishes, which yields the following governing equation for the steady di-
 161 mensionless flow depth, $h(x, y)$,

$$\frac{\partial h}{\partial x} = \mathcal{F} \nabla^2 h^2 / 2, \quad (10)$$

162 in both $r > 1$ and $r < 1$. On the cylinder boundary, the pressure and volume flux are
 163 continuous (provided that h is non-vanishing), which corresponds to

$$h^+ = h^-, \quad \text{and} \quad \cos \theta - \mathcal{F} \frac{\partial h^+}{\partial r} = \lambda \left(\cos \theta - \mathcal{F} \frac{\partial h^-}{\partial r} \right), \quad (11)$$

164 where θ is the polar angle and A^\pm denotes the value of A at $r = 1^\pm$. In the far-field,
 165 the flow depth returns to its uniform value ($h \rightarrow 1$ as $r \rightarrow \infty$).

166 In this study we integrate the system numerically and analyse it asymptotically to
 167 draw out the important behaviours. To solve the steady governing system numerically,
 168 we first reformulate it into a weak form. We multiply the equation for mass conserva-
 169 tion, $\nabla \cdot \mathbf{q} = 0$, by a test function v and integrate over the domain, Ω , to obtain

$$\int \int_\Omega k(r)h \left(1 - \mathcal{F} \frac{\partial h}{\partial x}, -\mathcal{F} \frac{\partial h}{\partial y} \right) \cdot \nabla v \, dx \, dy = \int_{x=L_2} k(r)h v \, dS. \quad (12)$$

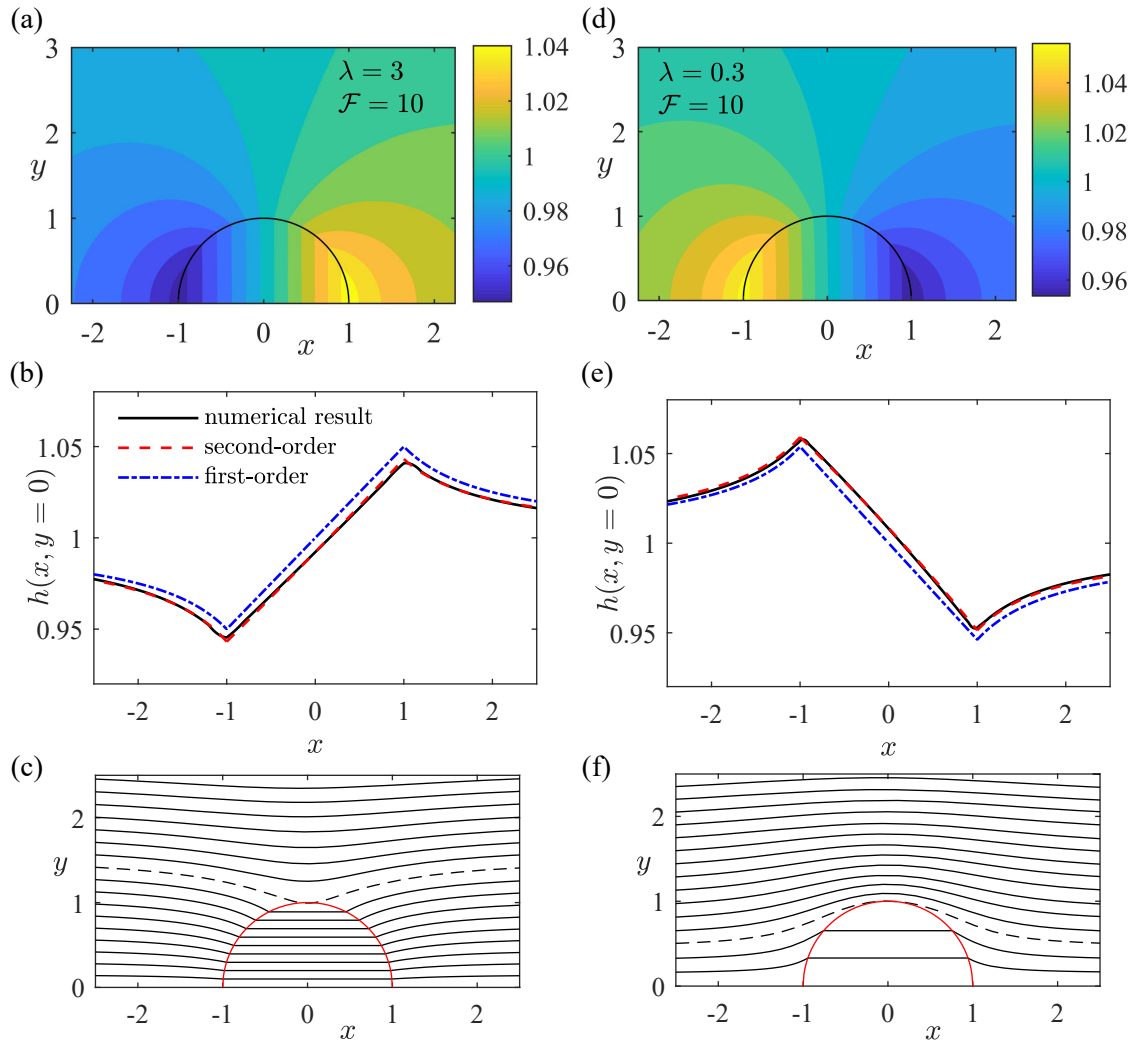


Figure 2: (a) Color plot of the thickness of the steady flow past a cylinder of relatively greater permeability, $\lambda = 3$, with $\mathcal{F} = 10$. (b) Flow thickness along the centreline, $y = 0$. (c) Particle paths through the cylinder from upstream. The dashed path just touches the cylinder. (d, e, f) Equivalent panels for $\lambda = 0.3$, with $\mathcal{F} = 10$.

170 We have used a rectangular domain, $\Omega = [-L_1, L_2] \times [0, L_3]$, where $L_i > 0$ and we
 171 have exploited the symmetry about $y = 0$ to reduce computational effort. We have also
 172 deployed the following boundary conditions: $\partial h / \partial y = 0$ on $y = 0, L_3$, $\partial h / \partial x = 0$ on
 173 $x = L_2$ and $h = 1$ on $x = L_1$. This variational problem is solved in FEniCS, which
 174 uses numerical finite elements to compute the solution (Petter Langtangen & Logg, 2017).
 175 The steady state is found iteratively; we take an initial guess to be $h = 1$ everywhere,
 176 corresponding to the case $\lambda = 1$ and iterate until a converged solution is found. The
 177 domain size is increased until the solution becomes independent of further increases to
 178 it. Typical values are $L_1 = 10$, $L_2 = 30$ and $L_3 = 10$. In the following sections, we
 179 analyse the dynamics of the flow in different regimes for the relative magnitude of \mathcal{F} and
 180 λ .

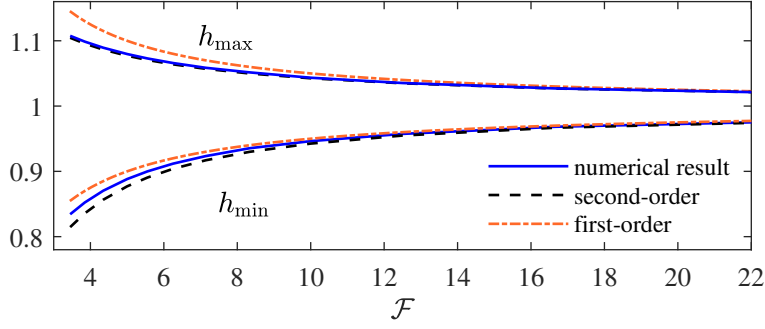


Figure 3: Maximum and minimum flow thickness for the steady flow through a cylinder of different permeability, with $\lambda = 3$. The asymptotic prediction (19) is plotted as a dashed line and the first order prediction, $h = 1 \pm \mathcal{F}^{-1}|1 - \lambda|/(1 + \lambda)$ is plotted as a dot-dashed line.

3 Relatively narrow cylinders ($\mathcal{F} \gg 1$)

To illustrate the solution for $\mathcal{F} \gg 1$ we plot the flow thickness for $\mathcal{F} = 10$ and two values of λ in figures 2a and 2d. In the case that the cylinder is less permeable than the exterior, the flow is deeper upstream and shallower downstream whilst the converse occurs in the case that the cylinder is more permeable than the exterior. Figure 2 also suggests that the flow thickness within the cylinder is approximately independent of the cross-slope coordinate y . We explore these observations more formally using asymptotic analysis.

For a relatively deep oncoming flow, we expect the cylindrical inclusion of a different permeability to perturb the flow depth only weakly because the induced pressure gradients associated with any height anomalies lead to flows which reduce them and this effect dominates the motion down the inclined impermeable surface (see figure 2). This motivates the expansion

$$h = 1 + \mathcal{F}^{-1}h_1 + \mathcal{F}^{-2}h_2 + \dots \quad (13)$$

On substituting (13) into (10) and equating at $O(\mathcal{F}^{-1})$, we find that the equation governing h_1 is given by

$$\nabla^2 h_1 = 0 \quad (14)$$

with boundary conditions $h_1 \rightarrow 0$ as $r \rightarrow \infty$ and

$$h_1^+ = h_1^-, \quad \text{and} \quad \frac{\partial h_1^+}{\partial r} - \lambda \frac{\partial h_1^-}{\partial r} = (1 - \lambda) \cos \theta, \quad \text{on } r = 1, \quad (15)$$

where the superscripts $+$ and $-$ denote evaluation at $r = 1^+$ and 1^- , respectively. The solution is given by

$$h_1 = \frac{\lambda - 1}{\lambda + 1} \begin{cases} r \cos \theta & r < 1 \\ r^{-1} \cos \theta & r > 1. \end{cases} \quad (16)$$

The solution is anti-symmetric about the y axis, which can be observed in the plots of the numerical results in figure 2. The flow depth predicted by the first-order expansion, $h = 1 + \mathcal{F}^{-1}h_1$, is compared with the numerical results along the centreline in figures 2b and 2e. A less permeable cylinder ($\lambda < 1$) leads to an increase in the flow thickness upstream of the cylinder because flow is diverted around it. Conversely, a more permeable cylinder ($\lambda > 1$) leads to a decrease in flow thickness upstream of the cylinder because the flow is focused into the cylinder.

To determine the next term in the expansion (13), h_2 , the solution in the region $r > 1$ requires matched asymptotic expansions to handle far-field divergences. The de-

208 tails are provided in the supplementary material, which adapts the method of Hinton
 209 et al. (2020). The inner solution, which is valid in $r < 1$, is given by

$$h_2 = \frac{\lambda - 1}{4(\lambda + 1)} \left\{ 2\gamma + 2 \log[1/(4\mathcal{F})] + \frac{r^2}{\lambda + 1} (2 + \cos 2\theta) \right\} \quad (17)$$

210 and in $r > 1$,

$$h_2 = \frac{\lambda - 1}{4(\lambda + 1)} \left\{ 2\gamma + 2 \log[r/(4\mathcal{F})] + \frac{\lambda(1 - r^{-2})(1 + \cos 2\theta) + 1 + \cos 2\theta + r^{-2}}{\lambda + 1} \right\}, \quad (18)$$

211 where $\gamma = 0.577\dots$ is Euler's constant. The flow thickness predicted by our asymp-
 212 totic expansions compares very favourably with the numerical results along the centre-
 213 line with $\mathcal{F} = 10$ in figure 2b for $\lambda = 3$ and figure 2e for $\lambda = 0.3$.

214 If the cylindrical inclusion is less permeable than the surroundings ($\lambda < 1$) then
 215 the flow attains its maximum depth at $r = 1$ and $\theta = \pi$ and its minimum value at $r =$
 216 1 and $\theta = 0$. The locations of the maxima and minima are interchanged for $\lambda > 1$. It
 217 is therefore possible to express the maxima and minima in compact form as

$$h_{\pm} = 1 \pm \mathcal{F}^{-1} \frac{|1 - \lambda|}{1 + \lambda} + \mathcal{F}^{-2} \frac{\lambda - 1}{2(\lambda + 1)} \left[\gamma + \frac{3}{2(\lambda + 1)} - \log(4\mathcal{F}) \right]. \quad (19)$$

218 This expression compares very favourably with our numerical results for the minimum
 219 and maximum flow thickness (figure 3, $\lambda = 3$). We note that the expansion (19) is valid
 220 for all λ even $\lambda \gg 1$ provided that $\mathcal{F} \gg 1$ because the magnitude of the expression
 221 $|1 - \lambda|/(1 + \lambda)$, which occurs in the second and third terms of (19), is at most 1.

222 3.1 Particle paths and flux into the cylinder

223 We use the results above to obtain the leading order velocity outside the cylinder
 224 ($r > 1$) for $\mathcal{F} \gg 1$,

$$\mathbf{u} = \left(1 + \frac{\lambda - 1}{\lambda + 1} \frac{\cos 2\theta}{r^2}, \frac{\lambda - 1}{\lambda + 1} \frac{\sin 2\theta}{r^2} \right) + \mathcal{O}(\mathcal{F}^{-1}), \quad (20)$$

225 whilst inside the cylinder,

$$\mathbf{u} = \left(\frac{2}{\lambda + 1}, 0 \right) + \mathcal{O}(\mathcal{F}^{-1}). \quad (21)$$

226 Hence the total dimensionless flux into (and out of) the cylinder is

$$\frac{4\lambda}{\lambda + 1} + \mathcal{O}(\mathcal{F}^{-1}) \quad (22)$$

227 This flux vanishes for an impermeable cylinder ($\lambda = 0$), is equal to 2 for an equal per-
 228 meability cylinder ($\lambda = 1$) and is at most 4 for a very permeable cylinder ($\lambda \rightarrow \infty$).

229 The particle paths to leading order for $\mathcal{F} \gg 1$ are shown in figure 2c and 2f for
 230 $\lambda = 3$ and $\lambda = 0.3$. By considering the flux (22), we can determine that fluid in the
 231 interval $|y| < 2\lambda/(\lambda + 1)$ from far upstream enters the cylinder (this region is denoted
 232 by a dashed line in figure 2c and figure 2f). The upstream region that is focused is at
 233 most $|y| < 2$ and hence particles outside this zone never pass through even the most
 234 permeable of cylinders.

235 Finally, we note that the leading order variation to the uniform depth, h_1 , deter-
 236 mines the perturbation to the hydrostatic pressure. Its governing equation is identical
 237 to the pressure field when the flow is driven in two-dimensions past a cylindrical inclu-
 238 sion by an imposed pressure difference (Bear, 1971).

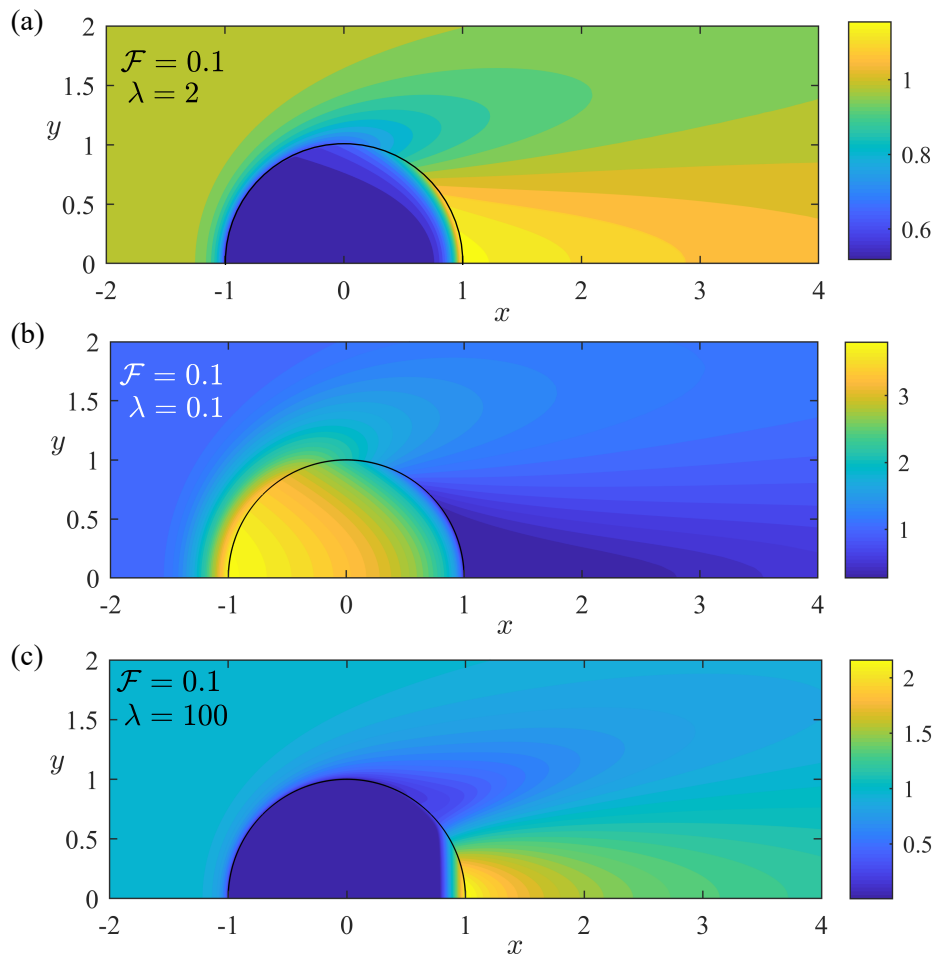


Figure 4: Thickness of the steady flow past a relatively wide cylindrical inclusion ($\mathcal{F} \ll 1$). The panels demonstrate the behaviour in the three regimes analysed in §§4, 5 and 6. Note the different colour scale in each plot.

4 Flow through a relatively wide cylinder [$\mathcal{F} \ll 1$, $\lambda = \mathcal{O}(1)$]

In the case of a relatively wide cylinder ($\mathcal{F} \ll 1$), qualitatively different behaviour occurs depending on the relative permeability of the cylindrical inclusion. We find that there are three possible regimes, which correspond to $\lambda \ll 1$, $\lambda = \mathcal{O}(1)$ and $\lambda \gg 1$ (see the panels in figure 4). In this section we analyse the middle case of similar permeabilities ($\lambda = \mathcal{O}(1)$). The flow is not significantly diverted by the cylinder and the velocity is equal to $(1, 0)$ to leading order outside the cylinder and $(\lambda, 0)$ inside the cylinder. The particle paths are nearly parallel to the x axis. Almost all the fluid emanating from $|y| < 1$ upstream flows into the cylinder. There is an abrupt change in the flow depth at $r = 1$ and this transition region is analysed in §4.1. Then, in §4.2 we show that diversion at the cylinder boundary becomes important when the inclusion is of very low or very high permeability and these cases are analysed in §5 and §6, respectively.

4.1 Asymptotic analysis for flow through the cylinder ($\lambda \sim 1$)

When a steady flow encounters a relatively wide cylindrical inclusion of similar permeability to the surrounding medium, mass conservation implies that the flow thickness inside the cylinder is $1/\lambda$ to leading order, while outside it is unity (see figure 4a). A narrow zone occurs around the edge of the cylinder in which the thickness transitions from one value to another. To examine the depth here we introduce a rescaled radial coordinate, $\xi = (r-1)/\mathcal{F}$ and write the flow depth interior and exterior to the cylinder as

$$h_{\text{int}} = h_{i0} + \mathcal{O}(\mathcal{F}), \quad h_{\text{ext}} = h_{e0} + \mathcal{O}(\mathcal{F}). \quad (23)$$

The leading order terms in the governing equation are then given by

$$\cos \theta \frac{\partial \hat{h}}{\partial \xi} = \frac{\partial}{\partial \xi} \left(\hat{h} \frac{\partial \hat{h}}{\partial \xi} \right), \quad (24)$$

where \hat{h} denotes either h_{i0} or h_{e0} . Outside of the transition zone, the flow depth, \hat{h} , matches to a far field value, namely $h_{i0} \rightarrow 1/\lambda$ as $\xi \rightarrow -\infty$ and $h_{e0} \rightarrow 1$ as $\xi \rightarrow \infty$. Conditions at the edge of the cylinder require that

$$h_{i0} = h_{e0} \quad \text{and} \quad \cos \theta - \frac{\partial h_{e0}}{\partial \xi} = \lambda \left(\cos \theta - \frac{\partial h_{i0}}{\partial \xi} \right) \quad \text{at} \quad \xi = 0. \quad (25)$$

We integrate (24) and apply the far-field conditions to find

$$\cos \theta (h_{e0} - 1) = h_{e0} \frac{\partial h_{e0}}{\partial \xi}, \quad \text{and} \quad \cos \theta (h_{i0} - 1/\lambda) = h_{i0} \frac{\partial h_{i0}}{\partial \xi}. \quad (26)$$

If $\cos \theta > 0$ (26a) requires that $h_{e0} = 1$ and then integrating (26b) and applying boundary conditions leads to

$$\xi \cos \theta = h_{i0} - 1 + \lambda^{-1} \log \left| \frac{h_{i0} - \lambda^{-1}}{1 - \lambda^{-1}} \right|. \quad (27)$$

Conversely if $\cos \theta < 0$ then we deduce that $h_{i0} = \lambda^{-1}$ and integrating (26a) yields

$$\xi \cos \theta = h_{e0} - \lambda^{-1} + \log \left| \frac{h_{e0} - 1}{\lambda^{-1} - 1} \right|. \quad (28)$$

The leading order expansions obtained here for the flow depth are favourably compared to the numerical results along the centreline in figure 5. A region in which the flow depth is deeper than predicted occurs at the downstream boundary in the case that $\lambda > 1$ (figure 5a). For large enough permeability contrasts, this deep region invalidates the asymptotic analysis as discussed in the next subsection. A similar breakdown occurs at the upstream boundary in the case that the inclusion is of much lower permeability than the exterior.

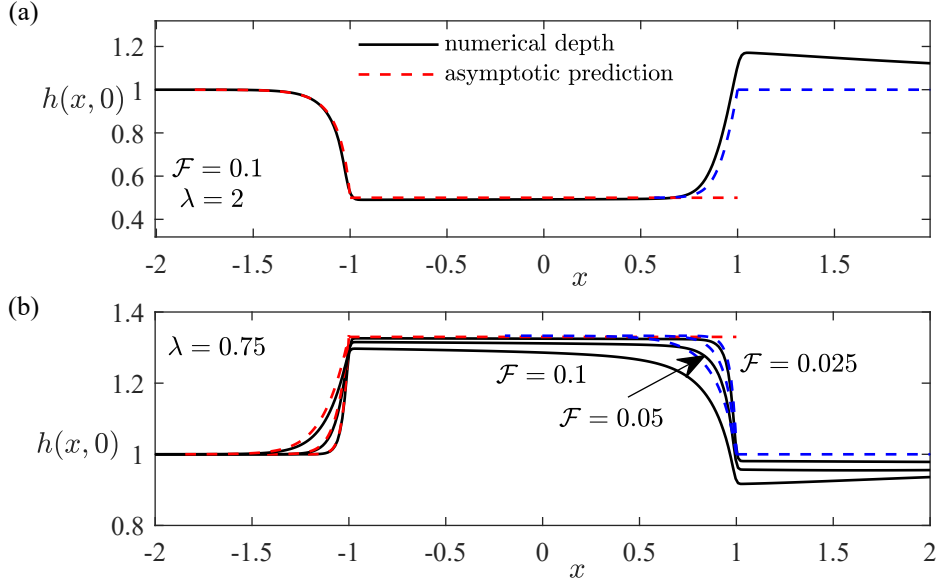


Figure 5: The steady flow thickness along the centreline for a relatively wide cylinder ($\mathcal{F} \ll 1$) with permeability of the same order of magnitude as the surrounding medium ($\lambda \sim 1$). The asymptotic predictions from §4.1 (red dashed lines upstream and blue dashed lines downstream) are compared to the numerical results (black lines). (a) $\lambda = 2$. (b) $\lambda = 0.75$.

273
274

4.2 Breakdown of the asymptotic analysis for cylinders of relatively low and high permeability

275
276
277
278
279
280
281
282
283
284
285
286
287

If the cylinder is of much lower permeability than the surrounding medium ($\lambda \ll 1$) then the gradient in the flow depth near $r = 1$, described above, is large (figure 4b). There is a deep region upstream of but close to the cylinder in which the flow around the boundary of the cylinder becomes important. For sufficiently small λ , the flow into this deep region is balanced predominantly by flow around the cylinder rather than flow into the cylinder (see figure 6a and figure 6b). In this case, the cylinder acts as an almost impermeable medium, an effect that might be accentuated by the inclusion of an entry pressure, and the asymptotic analysis in the preceding section is not valid. In the present subsection, we investigate how impermeable the cylinder needs to be, for a particular oncoming flow depth and cylinder width, for the flow to be predominantly diverted around the cylinder. Note that this diversion is also associated with increased flow thickness cross-stream of the cylinder in $1 < y < 1.5$ and decreased flow thickness downstream in $0 < y < 1$ (see figure 4b).

288
289
290
291

To obtain this relationship between \mathcal{F} and λ at which the transition between figure 6a and figure 6b occurs, we consider the flux around the cylinder predicted by the expansion for negligible diversion (28). Just upstream of but near to the cylinder ($\xi \ll 1$), the leading order flow depth can be obtained by linearising (28),

$$h_{e0} = \lambda^{-1} + (1 - \lambda)\xi \cos \theta, \quad (29)$$

292
293

which vanishes at $\xi = \bar{\xi}(\theta) = -1/[(1 - \lambda)\lambda \cos \theta]$. The tangential flux around the cylinder in the region close to the cylinder ($\xi \ll 1$) to leading order is

$$\mathcal{F} \int_{\xi=0}^{\xi=\bar{\xi}(\theta)} -h_{e0} u_{\theta} d\xi = \frac{-\lambda^{-2} \mathcal{F} \tan \theta}{2}, \quad (30)$$

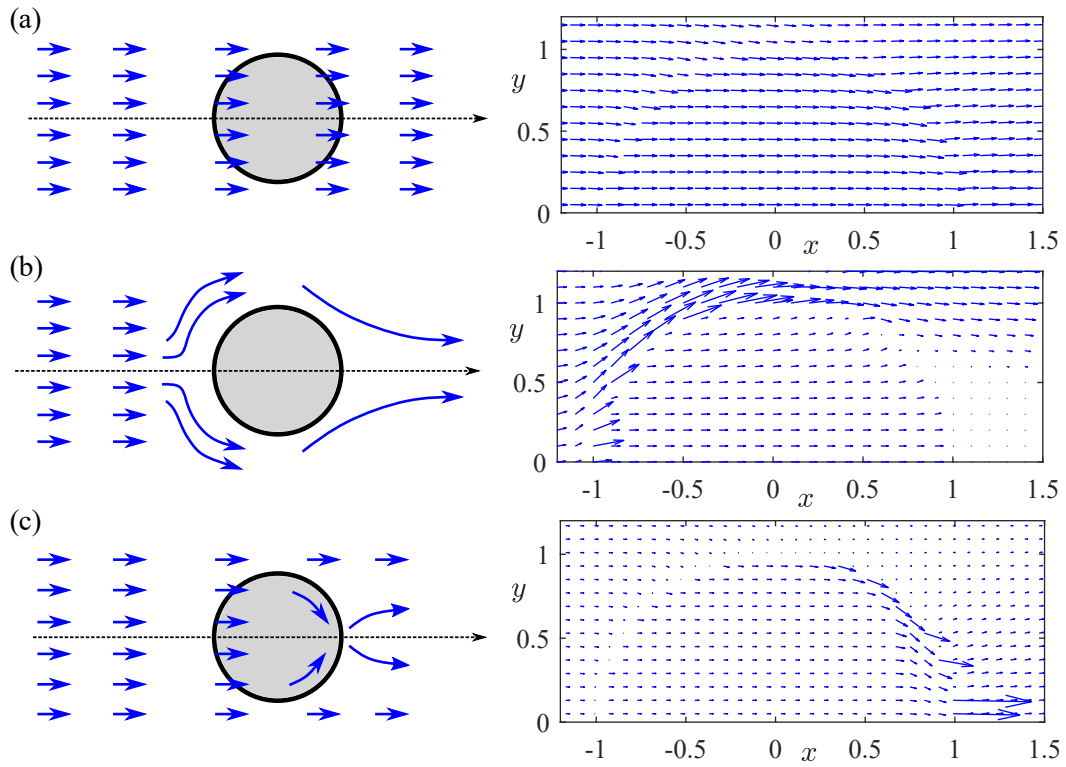


Figure 6: Schematics of the regimes for relatively shallow flow ($\mathcal{F} \ll 1$) past a circular cylindrical inclusion (left column) and corresponding plots of the flux vector, \mathbf{q} , obtained numerically (right column). (a) Inclusion permeability similar to the exterior ($\mathcal{F}^{1/2} \ll \lambda \ll \mathcal{F}^{-1}$). The flow is predominantly parallel to the downslope direction. The case $\lambda = 2$, $\mathcal{F} = 0.2$ is shown on the right. (b) Inclusion of low permeability ($\lambda \ll \mathcal{F}^{1/2}$); the flow is predominantly diverted around the cylinder ($\lambda = 0.15$, $\mathcal{F} = 0.05$ is shown). (c) Inclusion of high permeability ($\lambda \gg \mathcal{F}^{-1}$); the flow is diverted at the downstream boundary towards the centreline where a deep pond of fluid develops ($\lambda = 50$, $\mathcal{F} = 0.2$ is shown).

294 since the leading order term in the tangential velocity is $u_\theta = -\sin \theta$ and we have assumed that $\lambda \ll 1$. For the ‘negligible’ diversion regime to be self-consistent, the flux
 295 (30) must be much less than the flux into the cylinder, which is order 1, requiring $\mathcal{F}^{1/2} \ll$
 296 λ . Hence a transition occurs when $\lambda \sim \mathcal{F}^{1/2}$. The flow structure in the case of a relatively impermeable cylinder ($\lambda \ll \mathcal{F}^{1/2}$) is described in section 5 (see also figure 6b).
 297
 298

299 In the case that the cylinder is much more permeable than the surrounding medium, the analysis of the preceding section breaks down inside the cylinder near the downstream
 300 boundary. This is because the exterior is much less permeable and so the fluid within
 301 the cylinder is focused towards $x = 1, y = 0$ rather than flowing out of the cylinder
 302 along streamlines that are parallel to the downslope direction (see figure 6c). The focusing
 303 is associated with a reduced flow depth downstream of the cylinder along $y \approx 1$ and
 304 an increased flow depth downstream of the cylinder along the centreline towards which
 305 the flow is diverted (see figure 4c). To obtain the relationship between \mathcal{F} and λ at which
 306 the transition to this high permeability regime occurs, we apply a similar flux argument
 307 to that described above.
 308

309 According to the $\lambda \sim 1$ asymptotic analysis, the flow depth in the transition region inside the cylinder near the downstream boundary is given by equation (27). For
 310 large λ , we linearise the depth in this region to obtain
 311

$$h_{i0} = 1 + \xi \cos \theta. \quad (31)$$

312 This vanishes at $\xi = -1/\cos \theta$. The flux tangential to the boundary, just inside the cylinder is given by
 313

$$\mathcal{F} \int_{\xi=-1/\cos \theta}^{\xi=0} \lambda h_{i0} u_\theta d\xi. \quad (32)$$

314 The leading order term in the velocity is $u_\theta = -\sin \theta$ and we calculate that the tangential flux is
 315

$$\frac{-\lambda \mathcal{F} \tan \theta}{2}. \quad (33)$$

316 The asymptotic analysis in the previous subsection, where there is no diversion of the flow, is valid provided that this tangential flux is much smaller than the flux in the downslope
 317 direction, which is unity. In other words, there is no diversion provided that $\lambda \mathcal{F} \ll$
 318 1 but if $\lambda \gg \mathcal{F}^{-1}$ then the exterior behaves as almost impermeable relative to the inclusion and a different asymptotic expansion is needed at the downstream boundary (see
 319 §6). We conclude the present section by noting that the ‘negligible’ diversion behaviour, as described above, occurs provided that $\mathcal{F}^{1/2} \ll \lambda \ll \mathcal{F}^{-1}$, which corresponds to a
 320 sufficiently shallow oncoming flow (or sufficiently wide cylinder) and permeabilities that
 321 are sufficiently similar.
 322
 323
 324

325 **5 A relatively low permeability cylinder ($\lambda \ll \mathcal{F}^{1/2} \ll 1$)**

326 We analyse the diversion of flow around a relatively wide cylindrical inclusion ($\mathcal{F} \ll$
 327 1) that is of sufficiently low permeability relative to the exterior that the flux into the
 328 cylinder is negligible ($\lambda \ll \mathcal{F}^{1/2}$). We obtain the depth in $r > 1$ by assuming that the
 329 cylinder is impermeable to leading order. The flow outside the cylinder in the case of small
 330 but non-zero λ is similar to the flow for an impermeable cylinder ($\lambda = 0$), as demonstrated in figure 7b.
 331

332 Upstream of an impermeable cylinder, there is a ‘pond’ of fluid in which the radial velocity is zero owing to the no-flux condition (see Hinton et al., 2019, 2020),
 333

$$u_r = \cos \theta - \mathcal{F} \frac{\partial h}{\partial r} = 0. \quad (34)$$

334 Upon integrating we obtain the ‘pond’ depth,

$$h_p = \mathcal{F}^{-1}(r - 1) \cos \theta + g(\theta), \quad (35)$$

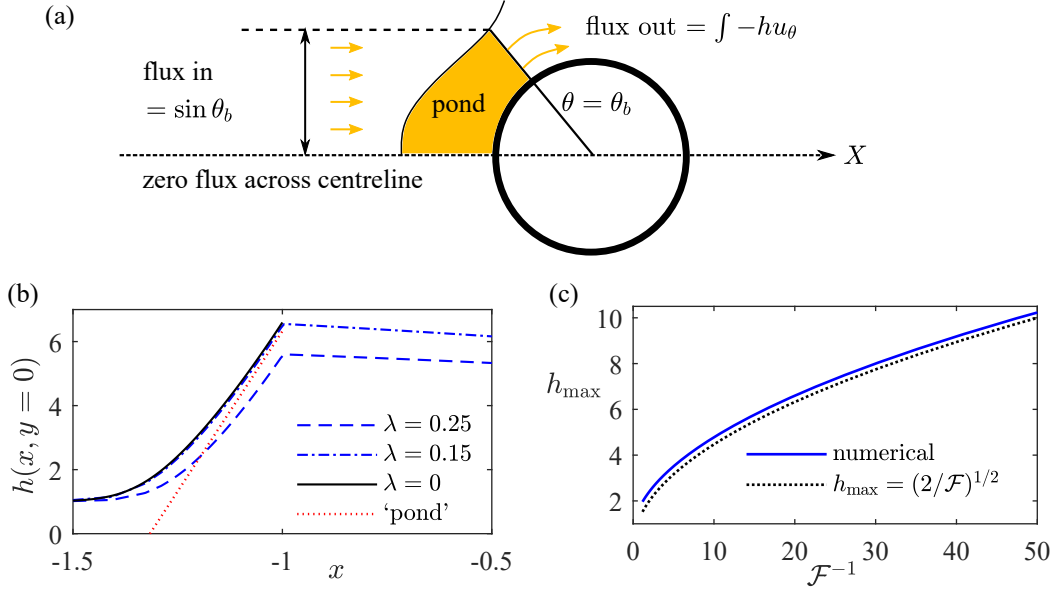


Figure 7: (a) Schematic illustrating the balance of flux in the pond. (b) Flow depth along the centreline for three values of λ with $\mathcal{F} = 0.05$. For $\lambda = 0$, the numerical solution was calculated using a no flux boundary condition at $r = 1$. The upstream asymptotic approximation (35) is shown in red dots. (c) Maximum flow thickness for the steady flow past an impermeable cylinder ($\lambda = 0$). The asymptotic approximation (39) is compared to the numerical results.

335 where $g(\theta)$ is a function of integration, which we determine by balancing the flux into
 336 and out of the pond (see figure 7a). The pond vanishes ($h_p = 0$) at $r = r_0(\theta) = 1 -$
 337 $\mathcal{F}g(\theta)/\cos\theta > 1$. The flow depth returns to $h \sim 1$ here. The flux into the pond be-
 338 tween $\theta = \pi$ and $\theta = \theta_b$ from upstream is $\sin\theta_b$ because the upstream flux is aligned
 339 with the x -axis and is unity, per unit width. The flux out of this region of the pond is
 340 provided by the tangential flux around the boundary at $\theta = \theta_b$,

$$\int_1^{r_0(\theta_b)} -hu_\theta dr = \int_1^{r_0(\theta_b)} h_p \sin\theta_b dr, \quad (36)$$

341 where we have ignored the term $(\mathcal{F}/r)\partial h/\partial\theta$ in the velocity because it is negligible for
 342 $\mathcal{F} \ll 1$, which can be confirmed a posteriori. Balancing the fluxes and substituting in
 343 (35) yields

$$\sin\theta_b = \int_1^{r_0(\theta_b)} [\mathcal{F}^{-1}(r-1)\cos\theta_b + g(\theta_b)] \sin\theta_b dr. \quad (37)$$

344 After some manipulation, we find that

$$g(\theta) = \mathcal{F}^{-1/2}(-2\cos\theta)^{1/2}. \quad (38)$$

345 The asymptotic prediction for the maximum flow depth, which occurs at $r = 1$, $\theta =$
 346 π , is given by

$$h_{\max} = 2^{1/2}\mathcal{F}^{-1/2}, \quad (39)$$

347 for $\mathcal{F} \ll 1$. We compare this expression (39) with the numerical results for the max-
 348 imum flow thickness in figure 7c. For $\lambda = 0$, a good empirical approximation for the
 349 maximum depth for all \mathcal{F} is $h_{\max} = (1+2/\mathcal{F})^{1/2}$ as shown in figure 1c (c.f. Hinton et
 350 al., 2020).

351 The leading order expression for the flow depth along the centreline upstream of
 352 the cylinder ($x < 1$) is given by (35), which accurately reproduces the numerical results
 353 for $\mathcal{F} = 0.05$ in figure 7b.

354 Finally, we comment on the validity of the lubrication model given that the flow
 355 has become relatively deep. Indeed the pond region has a large gradient in the free-surface
 356 but provided that $\tan \beta \ll 1$, the flow may still be approximated as shallow, for a full
 357 discussion see Lister (1992).

358 **6 A very permeable cylinder ($\lambda \gg \mathcal{F}^{-1} \gg 1$)**

359 In the regime $\lambda \gg \mathcal{F}^{-1} \gg 1$, the flow is focused towards the downstream trail-
 360 ing edge of the cylinder ($x = 1, y = 0$), where a deep pond of fluid forms (see figure
 361 4c and figure 8a). The analysis of §4.1 is valid upstream in $x < 0$ (see figure 8a). The
 362 regime transition occurs for large λ because the exterior acts as impermeable and a pond
 363 develops similar to the transition for small λ when the interior behaves as impermeable
 364 and a pond develops upstream in $r > 1$ (see figure 6b and figure 6c).

365 We find that for $\lambda \gg \mathcal{F}^{-1}$, there is additionally a relatively ‘shallow’ pond just
 366 upstream of the cylinder boundary and away from the centreline in which the bound-
 367 ary with the exterior appears impermeable. This corresponds to the spatial region $0 <$
 368 $1 - r \ll 1$ and $\theta = \mathcal{O}(1) < \pi/2$. We obtain the depth of this pond by balancing the
 369 flux from upstream with the flux tangential to the cylinder boundary. This shallow pond
 370 diverts fluid towards $x = 1, y = 0$, where there is a deeper pond, which we analyse
 371 by balancing the flux in from the shallow pond with the flux out of the cylinder.

372 We first analyse the flow thickness in the shallow pond. The exterior of the cylin-
 373 der is approximately impermeable, which suggests that a ponded region forms in which
 374 the free surface is horizontal and given by

$$h_s = \mathcal{F}^{-1}(r - 1) \cos \theta + m(\theta), \quad (40)$$

375 where $m(\theta)$ is a function that is to be determined. The region occupies

$$1 > r > r^*(\theta) = 1 - \mathcal{F}m(\theta)/\cos \theta. \quad (41)$$

376 We consider the flux balance in $[\theta, \pi/2]$. The flux from upstream within the cylinder into
 377 this region is $1 - \sin \theta$. There is no flux out of the cylinder and balancing this upstream
 378 flux with the flux tangential to the cylinder boundary out of the region yields

$$1 - \sin \theta = \lambda \int_{r^*}^1 h_s \sin \theta \, dr \quad (42)$$

379 where we have ignored the lower order contribution to the tangential velocity, $-(\mathcal{F}/r)\partial h/\partial \theta$,
 380 as it is negligible for $\mathcal{F} \ll 1$. Upon integrating and substituting for h_s , we obtain

$$m(\theta) = (\lambda \mathcal{F})^{-1/2} 2^{1/2} [(1 - \sin \theta) \cot \theta]^{1/2}. \quad (43)$$

381 Note that in the corresponding expression in $-\pi/2 < \theta < 0$, the 1 is replaced by -1 .
 382 The flow thickness in this pond is $h \sim (\lambda \mathcal{F})^{-1/2} \ll 1$. We note that the flux out of
 383 the cylinder in this region is $h \cos \theta$ to leading order owing to continuity at $r = 1$. Thus
 384 the flux leaving the inclusion is proportional to $(\lambda \mathcal{F})^{-1/2}$, which is much smaller than
 385 unity and consistent with the modelling assumption for this ponded region.

386 The pond prediction is compared to the numerical result for $\mathcal{F} = 0.1$ and $\lambda =$
 387 100 along the ray $\theta = \pi/4$ in figure 8b; the numerical result for $\lambda = 50$ is also included.
 388 The pond thickness is compared to the numerical result on the cylinder boundary ($r =$
 389 1) in figure 8c, which identifies that the present approximation is not accurate for $\theta \ll$

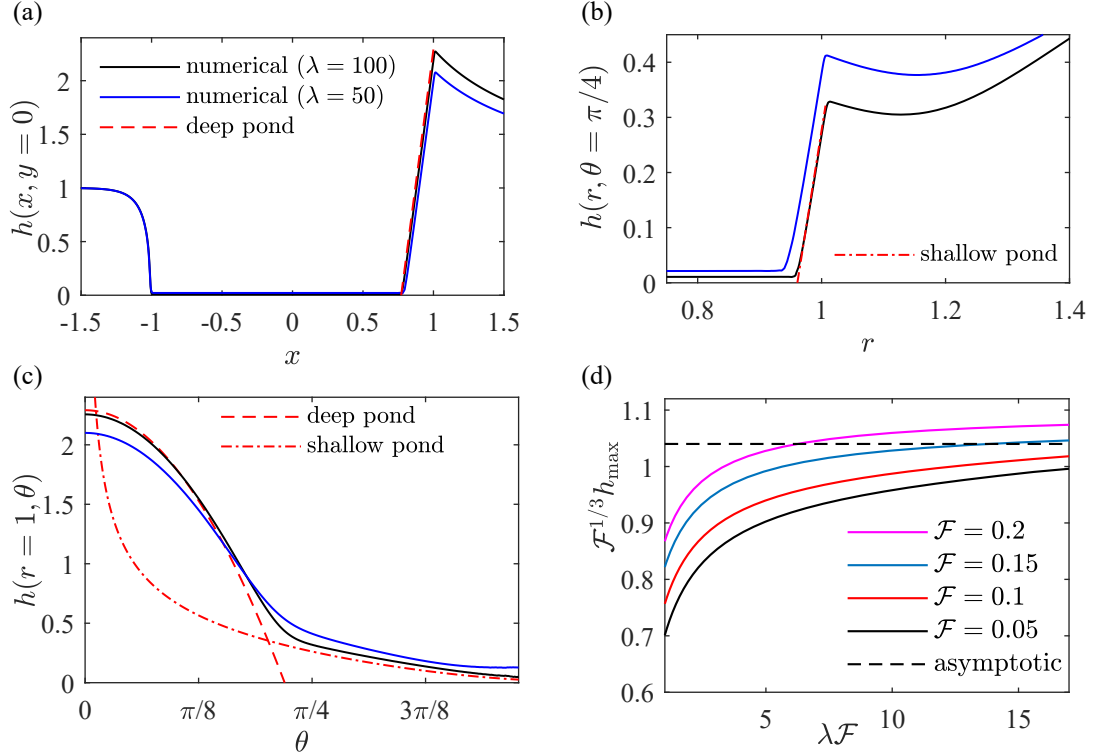


Figure 8: (a) Flow depth along the centreline with $\mathcal{F} = 0.1$. The asymptotic predictions are shown for $\lambda = 100$. (b) Flow depth along $\theta = \pi/4$. (c) Flow depth around the downstream boundary of the cylinder, $r = 1$, $0 < \theta < \pi/2$. (d) The maximum flow depth on rescaled axes. Numerical results for $\mathcal{F} = 0.05, 0.1, 0.15, 0.2$ are compared to the asymptotic prediction plotted as a dotted line (48).

390 1. Indeed, $m(\theta)$ is singular as $\theta \rightarrow 0$. A second deeper pond approximation is needed
 391 here, which also accounts for the drainage of fluid out of the cylinder.

392 To quantify the size and depth of the deeper pond region localised to $x = 1$, $y =$
 393 0 inside the cylinder, we again balance fluxes. The flow out of the cylinder occurs pre-
 394 dominantly through this deeper pond region and the flux into the cylinder in $y \geq 0$ is
 395 unity. Thus the flux out of the deeper pond is also unity. The flow thickness in the pond
 396 is given by

$$h_d = \mathcal{F}^{-1}(x - x_0), \quad (44)$$

397 which corresponds to a horizontal free surface. The constant, x_0 , is to be determined
 398 and we write $x_0 = \cos \theta_0$, where $\theta_0 \ll 1$ is the angular boundary of the pond region.
 399 The flux out of the pond is given by the radial flux just outside the cylinder at $r = 1^+$,
 400 which in the regime $\mathcal{F} \ll 1$ is given by

$$\int_0^{\theta_0} h_d \cos \theta \, d\theta \quad (45)$$

401 at leading order, where we have used continuity of the thickness, h , at $r = 1$. Then bal-
 402 ancing fluxes and integrating, we obtain

$$1 = \mathcal{F}^{-1} \left[\frac{\theta_0}{2} - \frac{\sin(2\theta_0)}{4} \right]. \quad (46)$$

403 Given that $\mathcal{F} \ll 1$, we expand to obtain $\theta_0 = 3^{1/3}\mathcal{F}^{1/3} + \mathcal{O}(\mathcal{F})$. The extent of the
 404 pond is given by

$$x_0 = \cos \theta_0 = 1 - (3^{2/3}/2)\mathcal{F}^{2/3} + \mathcal{O}(\mathcal{F}^{4/3}). \quad (47)$$

405 The maximum depth occurs at $x = 1, y = 0$ and is given by

$$h_{\max} = \frac{3^{2/3}}{2}\mathcal{F}^{-1/3} + \mathcal{O}(\mathcal{F}^{1/3}). \quad (48)$$

406 The prediction of the pond depth (44) shows good agreement with the numerical results
 407 along the centreline, $y = 0$, and along the cylinder boundary, $r = 1$, in figure 8a and
 408 figure 8c with $\lambda = 100$ and $\mathcal{F} = 0.1$. We compare our prediction for the maximum
 409 depth (48) to the numerical results in figure 8d. Each continuous line corresponds to a
 410 fixed value of \mathcal{F} , whilst λ is varied. The maximum flow depth becomes approximately
 411 independent of λ for $\lambda\mathcal{F} \gg 1$, in accord with our asymptotic theory. The error in $\mathcal{F}^{1/3}h_{\max}$
 412 between asymptotic theory and the numerical results is a small fixed constant, propor-
 413 tional to $\mathcal{F}^{2/3}$, as $\lambda \rightarrow \infty$.

414 7 Cylinders with non-circular cross-sections

415 Hitherto, we have restricted our attention to circular cylinders. It is interesting to
 416 extend this analysis to other cross-sections to understand how the shape affects the depth
 417 of the steady flow. We focus on the case of a relatively wide cylinder ($\mathcal{F} \ll 1$). The cal-
 418 culation in the case of a relatively narrow cylinder ($\mathcal{F} \gg 1$) reduces to the problem of
 419 two-dimensional potential flow in order to determine the perturbation to the upstream
 420 flow depth, $h = 1 + \mathcal{F}^{-1}h_1$ (see §3).

421 7.1 Kite cross-section cylinders

422 We analyse the interaction of the flow with a cylinder with a kite cross-section, sym-
 423 metric about the centreline. The vertices are at $(0, \pm 1)$ and $(\pm \cot \psi, 0)$ and the kite edges
 424 make an angle ψ with the centreline. The general behaviour is similar to the interaction
 425 with a circular cylinder and in what follows we highlight the key differences. For the regime
 426 in which there is little diversion of fluid ($\lambda \sim 1$), there are steep regions near the kite
 427 boundary within which the flow transitions from one depth to another, analogous to the
 428 behaviour for a circular cylinder. We show below that the relative size of λ and \mathcal{F} at the
 429 transitions between the three flow regimes are identical to the circular case by analysing
 430 the high and low permeability regimes.

431 7.1.1 Relatively low permeability cylinder ($\lambda \ll \mathcal{F}^{1/2}$)

432 We follow the argument for the low permeability circular cylinder and treat the in-
 433 terior as impermeable. A pond develops upstream of the upstream boundaries and we
 434 obtain its depth by balancing fluxes. We rotate coordinates with

$$x' = (x + \cot \psi) \cos \psi + y \sin \psi, \quad y' = -x \sin \psi + y \cos \psi \quad (49)$$

435 In these coordinates, the upstream boundary lies along $0 < x' < 1/\sin \psi, y' = \cos \psi$.

436 The pond depth upstream of the kite can be written as

$$h_p = -\mathcal{F}^{-1}(y' - \cos \psi) \sin \psi + G_R(x'; \psi). \quad (50)$$

437 The flux balance in the pond is

$$x' \sin \psi = \int_{\cos \psi}^{\cos \psi + \mathcal{F}G_R/\sin \psi} h_p \cos \psi \, dy' \quad (51)$$

438 and we obtain

$$G_R = \mathcal{F}^{-1/2} \left(\frac{2x' \sin^2 \psi}{\cos \psi} \right)^{1/2}. \quad (52)$$

439 The flow depth increases with distance downstream along the wall, x' , which contrasts
 440 with the case of a circular cylinder for which the maximum depth occurs at the upstream
 441 stagnation point. The scaling for the depth along the wall is $h \sim \mathcal{F}^{-1/2}$, which is iden-
 442 tical to that for a circular cylinder. In fact, this scaling is obtained for any cylinder with
 443 non-zero curvature at the upstream point because the pond depth arises from the bal-
 444 ance of the advective flux in with the advective flux out. The case of a perpendicular up-
 445 stream boundary is analysed in §7.2.

446 The maximum flow depth for the low permeability kite occurs near the cross-stream
 447 edge ($x' = 1/\sin \psi$) and is given by

$$h_{\max} = (2 \tan \psi)^{1/2} \mathcal{F}^{-1/2}. \quad (53)$$

448 The flux into the inclusion in this regime is proportional to $\lambda \mathcal{F}^{-1/2}$ so the analysis is con-
 449 sistent provided that $\lambda \ll \mathcal{F}^{1/2}$. Also, the present analysis breaks down for ψ close to
 450 $\pi/2$ (see §7.2).

451 **7.1.2 Relatively high permeability cylinder ($\lambda \gg \mathcal{F}^{-1}$)**

452 In the case of a relatively high permeability ratio ($\lambda \gg \mathcal{F}^{-1}$), there is a shallow
 453 pond just upstream of the downstream boundary and away from the centreline. The depth
 454 there is of order $(\mathcal{F}\lambda)^{-1/2}$ as in the case of a circular cylinder because the balance is the
 455 same. The flux out of the cylinder away from the centreline is proportional to $(\mathcal{F}\lambda)^{-1/2}$,
 456 which is small provided that $\lambda \gg \mathcal{F}^{-1}$.

457 The deep pond near the centreline has depth $h = \mathcal{F}^{-1}(x-x_0)$. At the downstream
 458 boundary we rotate coordinates with

$$\hat{x} = (x - \cot \psi) \cos \psi - y \sin \psi, \quad \hat{y} = x \sin \psi + y \cos \psi \quad (54)$$

459 In these coordinates, the downstream boundary lies along $-1/\sin \psi < \hat{x} < 0$, $\hat{y} = \cos \psi$.
 460 The pond depth is given by

$$h = \mathcal{F}^{-1}(\hat{x} \cos \psi + \hat{x}_0 \cos \psi) \quad (55)$$

461 The flux out of the cylinder is given by

$$\int_{-\hat{x}_0}^0 \mathcal{F}^{-1}(\hat{x} \cos \psi + \hat{x}_0 \cos \psi) \sin \psi d\hat{x} = 1. \quad (56)$$

462 We integrate and obtain $\hat{x}_0 = (2\mathcal{F})^{1/2}(\sin \psi)^{-1/2}$ and the maximum flow depth is

$$\mathcal{F}^{-1/2} 2^{1/2} (\sin \psi)^{-1/2} \cos \psi \quad (57)$$

463 Note the different depth scaling to the circular cylinder for which $h \sim \mathcal{F}^{-1/3}$ (see (48)).
 464 In fact, the depth scaling in the deep pond is sensitive to the detailed shape (unlike the
 465 scaling upstream of a relatively impermeable cylinder).

466 In the shallow pond, the flow depth is

$$h = \mathcal{F}^{-1} \hat{y} \sin \psi + (\lambda \mathcal{F})^{-1/2} (\hat{x} + 1/\sin \psi)^{1/2} \left(\frac{2 \sin^2 \psi}{\cos \psi} \right)^{1/2} \quad (58)$$

467 which has the same scaling as the circular cylinder. This scaling occurs for any down-
 468 stream boundary that is not perpendicular to the centreline.

469

7.2 Square cross-section cylinders

470

471

472

473

We consider a square cylinder occupying $-1 < x < 1$, $-1 < y < 1$. Plots of the steady flow thickness are shown in figure 9. In the case that there is little diversion of fluid, ($\lambda \sim 1$), there is a thin transition region, similar to that for a circular cylinder, near the upstream and downstream boundaries of the square.

474

7.2.1 Relatively low permeability cylinder ($\lambda \ll \mathcal{F}^{2/3}$)

475

476

477

478

479

480

The main difference to the circular case is that the flux out of the upstream pond arises from terms associated with hydrostatic pressure gradients (which are proportional to \mathcal{F}) rather than from the advective flux associated with gravity acting downslope. This is because the boundary is perpendicular to the slope direction. We treat the interior of the square as impermeable. The pond depth is given by $h = \mathcal{F}^{-1}(x + 1) + G_s(y)$. The flux balance in the pond is

$$1 = \frac{\partial}{\partial y} \left(\int_{\hat{x}}^1 -\mathcal{F}h \frac{\partial h}{\partial y} dx \right), \quad (59)$$

481

482

483

where $\hat{x} = -1 - \mathcal{F}G_s(y)$. We note that $G_s(1) = 0$ and $G'_s(0) = 0$ owing to the end of the pond at the corner of the square and symmetry about the centreline, respectively. This yields the following expression

$$G_s(y) = \mathcal{F}^{-2/3} [3(1 - y^2)]^{1/3}, \quad (60)$$

484

485

486

487

which is a different scaling for the flow depth to the low permeability circular cylinder. This prediction for the the maximum flow thickness is $h_{\max} = 3^{1/3} \mathcal{F}^{-2/3}$, which is compared to the numerical results in figure 9c. The square cylinder behaves as impermeable for $\lambda \ll \mathcal{F}^{2/3}$ (note the difference with the circular case).

488

7.2.2 Relatively high permeability cylinder

489

490

491

492

493

494

495

496

497

498

499

In the case that the square cylinder is of much higher permeability than the exterior, the negligible diversion regime described above, in which the flow is approximately parallel to the centreline, applies. This is in contrast to the behaviour for circular and kite cross-sections, where the behaviour associated with negligible diversion breaks down at high permeability ratios because the flow in the direction tangential to the downstream boundary becomes significant. However, for a square cross-section, the downstream boundary is perpendicular to the slope direction and a permeability contrast does not give rise to cross-slope flow here. Hence there is no distinct high permeability regime for the square and the negligible diversion results apply provided that $\lambda \gg \mathcal{F}^{2/3}$. This is demonstrated in figure 9b, where we have used $\lambda = 40$ and $\mathcal{F} = 0.1$ but the flow depth is approximately 1 at the downstream boundary.

500

501

502

503

504

At the cross-stream boundaries $y = \pm 1$, there is a transition in the depth from the interior value, $h = \lambda^{-1}$, to the exterior value, $h = 1$. Away from the corners at $x = \pm 1$, $y = 1$ (by a distance of greater order than \mathcal{F}), the motion is controlled by a balance of downslope advection and cross-slope diffusion. Therefore, the governing equation in the transition region around $y = 1$ is approximately,

$$\frac{\partial h}{\partial x} = \mathcal{F} \frac{\partial}{\partial y} \left(h \frac{\partial h}{\partial y} \right), \quad (61)$$

505

506

507

in $y > 1$ and $y < 1$ with boundary conditions of continuity of h and a jump in $\partial h / \partial y$ associated with λ at $y = 1$. This has a similarity solution with $\eta = (y - 1) / [\mathcal{F}(1 + x)]^{1/2}$ with $h(\eta)$ satisfying

$$-\frac{1}{2} \eta \frac{\partial h}{\partial \eta} = \frac{\partial}{\partial \eta} \left(h \frac{\partial h}{\partial \eta} \right), \quad (62)$$

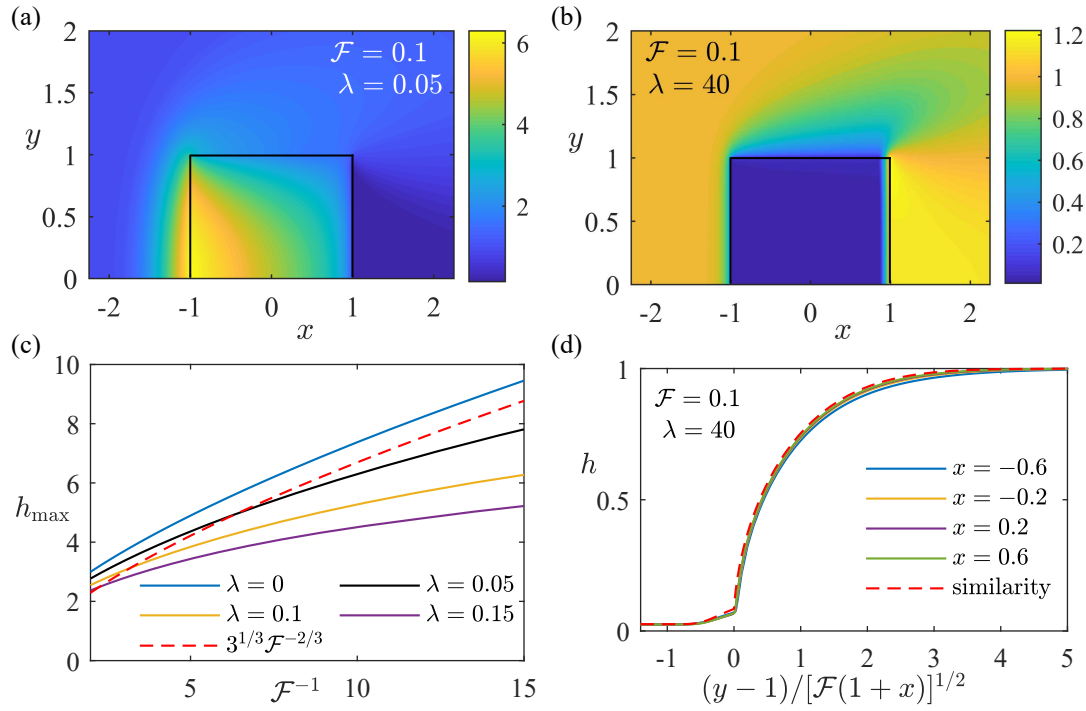


Figure 9: (a,b) Color plots of the thickness of the steady flow past a square cross-section inclusion (note the different depth scales). (c) The maximum flow thickness for low permeability square inclusions. (d) The self-similar behaviour in the cross-sectional flow depth near the cross-stream boundary of the square ($y = 1$) for $\lambda = 40$.

508 subject to continuity of h and $\lambda\partial h/\partial\eta^- = \partial h/\partial\eta^+$ at $\eta = 0$. We note that this self-
 509 similar transition behaviour also occurs in the ‘negligible’ diversion regime ($\lambda \sim 1$). The
 510 system (62) is integrated numerically and is compared to the numerical results in fig-
 511 ure 9d for $\lambda = 40$, demonstrating that the flow depth is approximately self-similar near
 512 the cross-stream boundary.

513 8 Discussion and application

514 We recall the two dimensionless parameters that govern the flow: $\lambda = K_i/K_o$ and
 515 $\mathcal{F} = H_\infty/(L \tan \beta)$. In the case that the cylinder is relatively narrow ($\mathcal{F} \gg 1$), the
 516 dimensionless flux into the cylinder is $4\lambda/(\lambda+1)$. The corresponding dimensional flux
 517 is

$$\frac{4K_i}{K_i + K_o} LQ. \quad (63)$$

518 The flux (63) is independent of the upstream depth, H_∞ and the slope gradient, $\tan \beta$
 519 (provided that $L \ll H_\infty/\tan \beta$) unlike the regime $\mathcal{F} \ll 1$. The particle paths are also
 520 independent of H_∞ and $\tan \beta$. This surprising result is related to the analogy between
 521 the $\mathcal{F} \gg 1$ regime and the case of pressure driven flow (for which there is no free-surface)
 522 described in §3.

523 We consider the common interaction between a CO₂ plume and an abandoned well
 524 (which may have been used for hydrocarbon recovery). We take the following typical pa-
 525 rameters: well radius of $L = 0.25$ metres, the permeability increases by a factor $\lambda =$
 526 1000 , the upstream plume thickness is $H_\infty = 3$ metres and the slope gradient is $\tan \beta =$
 527 0.01 (Celia et al., 2005). This yields $\mathcal{F} = 1200$. We calculate that the flow depth varies
 528 by less than a centimetre and fluid is drawn in from an upstream region of width one
 529 metre. Thus the depth is very slightly changed by the well but the particle paths are strongly
 530 diverted.

531 For a relatively wide cylinder ($\mathcal{F} \ll 1$), there are three sub-regimes depending on
 532 the permeability ratio, λ . For large permeability contrasts, ponds accumulate at either
 533 the downstream or upstream boundary. For example, consider a rectangular inclusion
 534 of cross-stream width $L = 200$ metres and much smaller permeability than the surround-
 535 ings so that effectively $\lambda = 0$, (e.g. figure 9 of Boggs et al. (1992) and Di Donato and
 536 Blunt (2004); Fitch et al. (2015)). Suppose that the inclusion is in a CO₂ storage site
 537 where the upstream depth is $H_\infty = 1$ metres and the slope is $\tan \beta = 0.02$. This in-
 538 clusion may only be a few metres thick in the z direction. We calculate $\mathcal{F} = 0.25$. The
 539 depth increases to approximately 4 metres upstream of the inclusion. If instead the in-
 540 clusion had twice the permeability of the exterior ($\lambda = 2$), then the depth within it would
 541 be approximately 0.5 metres near its upstream boundary but would gradually return to
 542 1 metre further downstream as fluid from the exterior flows across the sides of the in-
 543 clusion.

544 9 Conclusion

545 We have analysed the interaction of a gravitationally-driven free-surface flow in an
 546 inclined porous medium with a cylindrical inclusion of different permeability to the ex-
 547 terior. In the case that the cylinder is relatively narrow ($\mathcal{F} \gg 1$), we have obtained ex-
 548 pressions for the flux into the cylinder and the particle paths, which may be strongly di-
 549 verted or focused by the cylinder even though the free-surface is only weakly perturbed.

550 For relatively wide inclusions ($\mathcal{F} \ll 1$), we have found three qualitatively differ-
 551 ent regimes depending on the ratio, λ , of the internal and external permeabilities. In the
 552 case that the permeabilities are similar ($\lambda \sim 1$), the flow is everywhere parallel to the
 553 downstream direction. The flow thickness takes two approximately constant values in-
 554 side and outside the cylinder owing to mass conservation. The flow transitions in small

555 regions adjacent to the cylinder boundary. We have shown that the flow in the upstream
 556 transition zone diverts more flow around than into the cylinder when the cylinder is of
 557 lower permeability, $\lambda \ll \mathcal{F}^{1/2}$. The cylinder appears almost impermeable and a deep
 558 pond of fluid forms upstream with a horizontal free-surface and depth $h \sim \mathcal{F}^{-1/2}$. This
 559 scaling is general to cylinders with non-zero curvature at the upstream stagnation point.
 560 For the case of a square cylinder, the scaling for the depth in this pond is $h \sim \mathcal{F}^{-2/3}$
 561 instead.

562 The third regime for shallow oncoming flow occurs in the case of a high permeabil-
 563 ity cylinder. The transition away from the first regime is analogous to that for a low per-
 564 meability cylinder; the flux tangential to the downstream boundary just inside the cylin-
 565 der exceeds the flux out of the cylinder when $\lambda \gg \mathcal{F}^{-1}$. The flow is focused towards
 566 the rear side of the cylinder and there forms a pond of fluid within the cylinder at the
 567 rear. The flux out of the cylinder arises predominantly from the flow into and out of this
 568 pond. Interestingly, the flow depth in the pond becomes independent of the permeabil-
 569 ity contrast λ , when the latter is sufficiently large. Also, the flow depth in the pond is
 570 sensitive to the shape of the inclusion. Indeed, for a downstream boundary shape of the
 571 form $y = (1 - x)^{1/n}$ the deep pond has maximum depth $h \sim \mathcal{F}^{-a}$ where $a = -1/(1 +$
 572 $n)$. A kite corresponds to the case $n = 1$ and a circle corresponds to $n = 2$.

573 Our results provide insight into which of the various physical effects dominate in
 574 the interaction of free-surface porous flows with a single inclusion. It would be interest-
 575 ing to extend the analysis to an array of inclusions. Also, further study could focus on
 576 the transient evolution to the steady state such as investigating the role of capillary ef-
 577 fects at the invading front and calculating the time taken for the inclusion to be filled
 578 with fluid. Finally, the model presented here may be straightforwardly adapted to in-
 579 clude the effect of vertical leakage from within the inclusion through the underlying low
 580 permeability seal layer. This is manifest by an expression for mass loss in (10) associ-
 581 ated with leakage driven by the hydrostatic pressure (Acton et al., 2001; Pritchard &
 582 Hogg, 2002; Neufeld et al., 2011). We briefly comment that in this scenario for relatively
 583 narrow cylinders ($\mathcal{F} \gg 1$), the flow depth is not changed at leading order; it still given
 584 by $h = 1 + \mathcal{F}^{-1}h_1$, although h_1 takes a different form. For relatively wide cylinders,
 585 the maximum vertical leakage flux out of the cylinder is bounded above by the flux into
 586 the cylinder from the calculations described in this paper.

587 Acknowledgments

588 E.M.H. is grateful to the London Mathematical Society and the Heilbronn Institute for
 589 Mathematical Research for the award of an Early Career Research Fellowship (ref: ECF-
 590 1920-82).

591 This article has no additional data.

592 References

- 593 Acton, J. M., Huppert, H. E., & Worster, M. G. (2001). Two-dimensional viscous
 594 gravity currents flowing over a deep porous medium. *Journal of Fluid Mechan-*
 595 *ics*, *440*, 359–380. doi: 10.1017/S0022112001004700
- 596 Bachu, S. (2015). Review of CO2 storage efficiency in deep saline aquifers. *Inter-*
 597 *national Journal of Greenhouse Gas Control*, *40*, 188–202. doi: 10.1016/j.ijggc
 598 .2015.01.007
- 599 Barlow, P. M., & Reichard, E. G. (2010). Saltwater intrusion in coastal regions of
 600 North America. *Hydrogeology Journal*, *18*(1), 247–260. doi: 10.1007/s10040
 601 -009-0514-3
- 602 Bear, J. (1971). *Dynamics of flow in porous media*. Elsevier.
- 603 Bear, J., & Ryzhik, V. (1998). On the displacement of NAPL lenses and plumes in
 604 a phreatic aquifer. *Transport in porous media*, *33*(3), 227–255. doi: 10.1023/A:

- 1006544629038
- 605
606 Boggs, J. M., Young, S. C., Beard, L. M., Gelhar, L. W., Rehfeldt, K. R., & Adams,
607 E. E. (1992). Field study of dispersion in a heterogeneous aquifer: 1. Overview
608 and site description. *Water Resources Research*, *28*(12), 3281–3291. doi:
609 10.1029/92WR01756
- 610 Celia, M. A., Bachu, S., Nordbotten, J. M., Gasda, S. E., & Dahle, H. K. (2005).
611 Quantitative estimation of CO₂ leakage from geological storage: Analytical
612 models, numerical models, and data needs. *Greenhouse Gas Control Technolo-*
613 *gies* *7*, 663–671. doi: 10.1016/B978-008044704-9/50067-7
- 614 Chiquet, P., Daridon, J.-L., Broseta, D., & Thibeau, S. (2007). CO₂/water in-
615 terfacial tensions under pressure and temperature conditions of CO₂ geo-
616 logical storage. *Energy Conversion and Management*, *48*(3), 736–744. doi:
617 10.1016/j.enconman.2006.09.011
- 618 Dagan, G. (1984). Solute transport in heterogeneous porous formations. *Journal of*
619 *Fluid Mechanics*, *145*, 151–177. doi: 10.1017/S0022112084002858
- 620 Dagan, G., & Zeitoun, D. (1998). Free-surface flow toward a well and interface
621 upconing in stratified aquifers of random conductivity. *Water Resources Re-*
622 *search*, *34*(11), 3191–3196. doi: 10.1029/98WR02039
- 623 Di Donato, G., & Blunt, M. J. (2004). Streamline-based dual-porosity simulation of
624 reactive transport and flow in fractured reservoirs. *Water Resources Research*,
625 *40*(4). doi: 10.1029/2003WR002772
- 626 Eames, I., & Bush, J. (1999). Longitudinal dispersion by bodies fixed in a poten-
627 tial flow. *Proceedings of the Royal Society of London. Series A: Mathematical,*
628 *Physical and Engineering Sciences*, *455*(1990), 3665–3686. doi: 10.1098/rspa
629 .1999.0471
- 630 Fitch, P. J., Lovell, M. A., Davies, S. J., Pritchard, T., & Harvey, P. K. (2015). An
631 integrated and quantitative approach to petrophysical heterogeneity. *Marine*
632 *and Petroleum Geology*, *63*, 82–96. doi: 10.1016/j.marpetgeo.2015.02.014
- 633 Guo, B., Zheng, Z., Bandilla, K. W., Celia, M. A., & Stone, H. A. (2016). Flow
634 regime analysis for geologic CO₂ sequestration and other subsurface fluid in-
635 jections. *International Journal of Greenhouse Gas Control*, *53*, 284–291. doi:
636 10.1016/j.ijggc.2016.08.007
- 637 Hannis, S., Chadwick, A., Jones, D., Pearce, J., White, J., Connelly, D., . . . White,
638 P. (2015). *Review of offshore monitoring for CCS projects*. IEAGHG.
- 639 Hewitt, D. R., Peng, G. G., & Lister, J. R. (2020). Buoyancy-driven plumes in a lay-
640 ered porous medium. *Journal of Fluid Mechanics*, *883*. doi: 10.1017/jfm.2019
641 .888
- 642 Hinch, E. J., & Bhatt, B. S. (1990). Stability of an acid front moving through
643 porous rock. *Journal of Fluid Mechanics*, *212*, 279–288. doi: 10.1017/
644 S0022112090001963
- 645 Hinton, E. M., Hogg, A. J., & Huppert, H. E. (2019). Interaction of viscous free-
646 surface flows with topography. *Journal of Fluid Mechanics*, *876*, 912–938. doi:
647 10.1017/jfm.2019.588
- 648 Hinton, E. M., Hogg, A. J., & Huppert, H. E. (2020). Viscous free-surface flows past
649 cylinders. *Physical Review Fluids*, *5*(8), 084101. doi: 10.1103/PhysRevFluids.5
650 .084101
- 651 Hinton, E. M., & Woods, A. W. (2019). The effect of vertically varying permeability
652 on tracer dispersion. *Journal of Fluid Mechanics*, *860*, 384–407. doi: 10.1017/
653 jfm.2018.891
- 654 Huppert, H. E., & Woods, A. W. (1995). Gravity-driven flows in porous layers.
655 *Journal of Fluid Mechanics*, *292*, 55–69. doi: 10.1017/S0022112095001431
- 656 Kuila, U., & Prasad, M. (2013). Specific surface area and pore-size distribution in
657 clays and shales. *Geophysical Prospecting*, *61*(2-Rock Physics for Reservoir Ex-
658 ploration, Characterisation and Monitoring), 341–362. doi: 10.1111/1365-2478
659 .12028

- 660 Lister, J. R. (1992). Viscous flows down an inclined plane from point and
661 line sources. *Journal of Fluid Mechanics*, *242*, 631–653. doi: 10.1017/
662 S0022112092002520
- 663 MacFarlane, D. S., Cherry, J. A., Gillham, R. W., & Sudicky, E. A. (1983). Migra-
664 tion of contaminants in groundwater at a landfill: A case study: 1. Ground-
665 water flow and plume delineation. *Journal of Hydrology*, *63*(1-2), 1–29. doi:
666 10.1016/0022-1694(83)90221-4
- 667 Masterson, J. P., Walter, D. A., & LeBlanc, D. R. (1998). *Delineation of contribut-*
668 *ing areas to selected public-supply wells, western Cape Cod, Massachusetts*
669 (Vol. 98) (No. 4237). US Department of the Interior, US Geological Survey.
- 670 Mathieson, A., Midgely, J., Wright, I., Saoula, N., & Ringrose, P. (2011). In
671 Salah CO2 Storage JIP: CO2 sequestration monitoring and verification tech-
672 nologies applied at Krechba, Algeria. *Energy Procedia*, *4*, 3596–3603. doi:
673 10.1016/j.egypro.2011.02.289
- 674 Neufeld, J. A., Vella, D., Huppert, H. E., & Lister, J. R. (2011). Leakage from
675 gravity currents in a porous medium. Part 1. A localized sink. *Journal of Fluid*
676 *Mechanics*, *666*, 391–413. doi: 10.1017/S002211201000488X
- 677 Nordbotten, J. M., Celia, M. A., & Bachu, S. (2004). Analytical solutions for leak-
678 age rates through abandoned wells. *Water Resources Research*, *40*(4). doi: 10
679 .1029/2003WR002997
- 680 Petter Langtangen, H., & Logg, A. (2017). *Solving PDEs in Python: The FEniCS*
681 *Tutorial I*. Springer. doi: 10.1007/978-3-319-52462-7
- 682 Phillips, O. M. (1991). *Flow and reactions in permeable rocks*. Cambridge University
683 Press.
- 684 Pritchard, D. (2007). Gravity currents over fractured substrates in a porous
685 medium. *Journal of Fluid Mechanics*, *584*, 415–431. doi: 10.1017/
686 S0022112007006623
- 687 Pritchard, D., & Hogg, A. J. (2002). Draining viscous gravity currents in
688 a vertical fracture. *Journal of Fluid Mechanics*, *459*, 207–216. doi:
689 10.1017/S0022112002008327
- 690 Purcell, W. (1949). Capillary pressures—their measurement using mercury and the
691 calculation of permeability therefrom. *Journal of Petroleum Technology*, *1*(02),
692 39–48. doi: 10.2118/949039-G
- 693 Rezaeyan, A., Tabatabaei-Nejad, S. A., Khodapanah, E., & Kamari, M. (2015).
694 A laboratory study on capillary sealing efficiency of Iranian shale and an-
695 hydrite caprocks. *Marine and Petroleum Geology*, *66*, 817–828. doi:
696 10.1016/j.marpetgeo.2015.07.022
- 697 Sahu, C. K., & Flynn, M. (2017). The effect of sudden permeability changes in
698 porous media filling box flows. *Transport in Porous Media*, *119*(1), 95–118.
699 doi: 10.1007/s11242-017-0875-3
- 700 Sekhar, G. P. R., & Sano, O. (2001). Two-dimensional viscous flow past a slightly
701 deformed circular cavity in a porous medium. *Fluid Dynamics Research*, *28*(4),
702 281. doi: 10.1016/S0169-5983(00)00033-2
- 703 Stalker, L., Boreham, C., Underschultz, J., Freifeld, B., Perkins, E., Schacht, U.,
704 & Sharma, S. (2015). Application of tracers to measure, monitor and verify
705 breakthrough of sequestered CO2 at the CO2CRC Otway Project, Victoria,
706 Australia. *Chemical Geology*, *399*, 2–19. doi: 10.1016/j.chemgeo.2014.12.006
- 707 Vella, D., & Huppert, H. E. (2006). Gravity currents in a porous medium
708 at an inclined plane. *Journal of Fluid Mechanics*, *555*, 353–362. doi:
709 10.1017/S0022112006009578
- 710 Werth, C. J., Cirpka, O. A., & Grathwohl, P. (2006). Enhanced mixing and re-
711 action through flow focusing in heterogeneous porous media. *Water Resources*
712 *Research*, *42*(12). doi: <https://doi.org/10.1029/2005WR004511>
- 713 Woods, A. W., & Farcas, A. (2009). Capillary entry pressure and the leakage of
714 gravity currents through a sloping layered permeable rock. *Journal of Fluid*

715 *Mechanics*, 618, 361–379. doi: 10.1017/S0022112008004527
716 Woods, A. W., & Norris, S. (2010). On the role of caprock and fracture zones in dis-
717 persing gas plumes in the subsurface. *Water Resources Research*, 46(8). doi:
718 10.1029/2008WR007568